Journal of Materials Chemistry A

ROYAL SOCIETY OF CHEMISTRY

PAPER

View Article Online
View Journal | View Issue

Cite this: J. Mater. Chem. A, 2024, 12, 20288

The role of zwitterionic crosslinks in facilitating ion conduction, lithium deposition, and stable interface formation for polymer electrolyte-based lithium metal batteries†

Liang Chai,[abc] Zhiheng Zou,[abc] Zhengsheng Yang[abc] and Guang Yang *[abc]

Developing flexible polymer electrolytes that can concurrently promote ion conduction, uniform Li deposition, and robust solid electrolyte interphase (SEI) formation is promising for the development of next-generation lithium metal batteries (LMBs). Herein, a new polymeric zwitterionic electrolyte with a glass fiber support was investigated. A sulfobetaine zwitterionic crosslinker participated in *in situ* UV-triggered photopolymerization with a carbonate monomer and ether type dimethacrylate. The zwitterionic gel electrolyte (ZGE) demonstrated a high ionic conductivity exceeding 1×10^{-3} S cm^{-1} and electrochemical oxidative stability (>5 V *vs.* Li$^+$/Li). The zwitterionic crosslinker in the ZGE was able to mediate homogeneous Li$^+$ flux toward the lithium anode and suppress lithium dendrites (the Li/ZGE/Li cell can cycle stably for more than 1400 h with a current density of 0.1 mA cm^{-2}). The ZGE also helped construct a LiF-rich SEI favorable for dendrite suppression. A Li/ZGE/$LiFePO_4$ (LFP) cell demonstrated excellent long-term cycling stability (>600 cycles with a capacity retention of 92%, high discharge capacity of 155 mA h g^{-1}, and coulombic efficiency of >99.5%). The ZGE could also support a Li/$Ni_{0.815}Co_{0.15}Al_{0.035}O_2$ (NCA) cell to operate with a high specific capacity of 232 mA h g^{-1}. The flexible ZGE made it possible for a pouch-type Li/LFP cell to cycle and function well in a flat and bending state. This polymer electrolyte holds great promise for the exploration of high-energy polymeric LMBs.

Received 26th April 2024
Accepted 28th June 2024

DOI: 10.1039/d4ta02898h

rsc.li/materials-a

1. Introduction

Lithium ion batteries (LIBs) have been widely applied in consumer portable electronic devices and electrical vehicles and are being developed further for grid-scale storage.[1] The use of LIBs is expected to grow exponentially in the next decade.[2,3] However, as the requirement for the high safety and energy density of LIBs keeps increasing, commercial LIBs using graphite anodes and flammable liquid electrolytes cannot meet these demands. Consequently, the further scaling up of LIBs is impeded. However, next-generation lithium metal batteries (LMBs) are quite promising because lithium metal has a high theoretical capacity (3860 mA h g^{-1}) and the lowest electrochemical potential (−3.04 V *vs.* standard hydrogen electrode).[4,5]

Nevertheless, the high activity and volume effect of the lithium metal anode give rise to solid electrolyte interphase (SEI) fragmentation and dendritic lithium growth, which significantly restrict the practical application of the lithium metal anode. In order to address these issues, researchers have tried different attempts, such as modification of the lithium metal anode, surface protection techniques, and novel electrolyte design.[6] Firstly, for the modification of lithium metal, efforts have been dedicated to optimizing its composition and structure. For instance, utilizing {100} crystal orientation for Li can lower the surface energy/surface diffusion barrier, thereby enabling the uniform deposition of Li$^+$.[7,8] Additionally, employing structured lithium metal negative electrodes (composite lithium electrodes) with three-dimensional frames composed of dispersed and combined lithium metals offers improved controllability and safety. However, composite lithium electrodes still face several key drawbacks, including thickness control issues, density regulation problems, surface stability concerns, and lithophile adjustment difficulties.[9] It is worth mentioning that among these methods, the design of electrolytes has received increasing attention as electrolytes are responsible for Li$^+$ transport and directly affect the performance of the battery.[10] An unstable SEI formed by irreversible interfacial reactions between the liquid electrolyte and active lithium

[a]School of Electronic Science and Engineering, University of Electronic Science and Technology of China, Chengdu, 611731, China. E-mail: yg028@uestc.edu.cn
[b]National Engineering Research Center of Electromagnetic Radiation Control Materials, University of Electronic Science and Technology of China, Chengdu, 611731, China
[c]Key Laboratory of Multi-spectral Absorbing Materials and Structures of Ministry of Education, University of Electronic Science and Technology of China, Chengdu, 611731, China

† Electronic supplementary information (ESI) available: ^{1}H NMR, ^{13}C NMR, TG, EIS and so on. See DOI: https://doi.org/10.1039/d4ta02898h

metal often leads to lithium dendrite growth and "dead" lithium, which result in serious battery safety issues.[11]

In order to solve these problems, utilizing solid polymer electrolytes appears to be a quite promising approach because of their physicochemical advantages, such as satisfactory flexibility, light weight, and ease of processing.[12,13] Polyethylene oxide (PEO) has dominated in polymer electrolytes studies ever since Fenton *et al.* found that a mixture of PEO and salts such as NaI and KSCN with a low lattice energy was ion conductive.[14] Thereafter, PEO/lithium salt systems were extensively investigated.[15,16] However, considering their practical application in lithium batteries, PEO electrolytes do not have enough ionic conductivity (σ) or are able to form a stable SEI against lithium metal.[17] Thus, in order to improve the ion transport and interfacial stability of the polymer electrolyte against the lithium anode, various methods have been designed and explored.[18,19] Chemical modification (for example, copolymerization,[20] crosslinking,[21] fluorination[22]) of the polymer structure or introducing other benign additives/plasticizers[23] often disrupts the polymer chain regularity, reduces crystallization, improves ion conduction, and enhances the electrochemical stability window. In addition, it is known that a LiF-rich SEI is able to effectively suppress lithium dendrite growth and improve lithium deposition.[24] LiF usually originates from the decomposition of lithium salt and fluorine-containing carbonates.[25] It is desired that the polymer electrolyte cannot only effectively conduct Li^+ but also favor the homogeneous deposition of Li^+ on the anode and a stable SEI formation, which is essential for long-term battery cycling.[26,27] Zwitterionic molecules are a unique class of locally charged but overall neutral molecules, in which positive and negative charged atoms are covalently connected. Their strong dipole moments generated by the zwitterionic molecular structure can promote the dissolution of lithium salt.[28–30] This type of molecule could also interact with anions as well to adjust ion distribution.[31] Zwitterionic molecules have also been covalently linked to polymer chains to prepare zwitterionic polymers.[32] Crosslinking is a straightforward way to regulate the polymer chain segmental motion and improve the mechanical integrity of polymer electrolytes. It cannot only increase the amorphous region but also enhance the mechanical properties of a polymer electrolyte membrane.[33] Crosslinked zwitterionic polymer electrolytes are usually achieved by a copolymerization with zwitterionic monomers and neutral crosslinkers.[20,34,35] To the best of our knowledge, there has been no published work reporting a zwitterionic polymer electrolyte network, in which the zwitterionic structure exists within the crosslinker, in LMBs research. It would be of significant interest to know whether this type of polymer electrolyte could synergistically promote ion transport and enhance the electrode/electrolyte interfacial properties.

In this present work, a novel zwitterionic polymer electrolyte network was designed, prepared, and studied for LMBs. Here, a small amount of the zwitterionic crosslinker 3-(*N*,*N*-diallyl-*N*-methylammonio) propanesulfonate (DMA-SO_3^-) participated in a UV-initiated free radical copolymerization with vinyl ethylene carbonate (VEC) and poly(ethylene glycol) dimethacrylate (PEGDMA) in the presence of lithium bis(trifluoromethanesulfonyl) imide (LiTFSI) dissolved in fluorine-containing carbonates with a glass fiber support. The prepared electrolyte was named as a zwitterionic gel electrolyte (ZGE). ZGE was highly ion conductive, with σ reaching the 1×10^{-3} S cm^{-1} level at 30 °C. It also possessed a electrochemical oxidation potential (>5 V *vs.* Li^+/Li). The plating/stripping test of a fabricated Li/ZGE/Li cell and related characterizations proved that ZGE could efficiently suppress lithium dendrite growth. The lithium surface SEI chemistry demonstrated that ZGE with a uniformly distributed zwitterion structure could facilitate the formation of a LiF-rich SEI on the lithium anode. The Li/$LiFePO_4$(LFP) cell assembled with ZGE provided a reversible high discharge capacity of 155 mA h g^{-1} at 1C and good cycle stability (92% capacity retention after 600 cycles at 1C). The Li/$LiNi_{0.815}Co_{0.15}Al_{0.035}O_2$ (NCA) cell using ZGE demonstrated its ability to deliver a high specific capacity. Tests with the cyclable Li/LFP flexible/bendable pouch cell with ZGE highlight its potential for developing safe and flexible lithium batteries.

2. Results and discussion

2.1 Design and physicochemical structure characteristics of ZGE

The zwitterionic gel electrolyte (ZGE) was prepared by a facile UV-triggered polymerization. As shown in Fig. 1, a zwitterionic crosslinker (DMA-SO_3^-), ion coupling comonomer (VEC), and crosslinker (PEGDMA) in specific amounts were fully dissolved in a pre-prepared solution of 1 M LiTFSI in FEC/DMC (1 : 4, v/v) to form the precursor solution. Then the precursor solution was dropped onto a glass fiber mesh (GFM) before UV irradiation was applied. The process could also take place *in situ* on the surface of a lithium anode followed by cell assembly. Also, the precursor-solution-loaded GFM could also be cured elsewhere for characterization purposes. Several groups of electrolyte samples were prepared for the following study. The electrolyte that did not contain DMA-SO_3^- was named GE, The ZGE samples that incorporated 3 wt% of DMA-SO_3^-, 5 wt% DMA-SO_3^-, and 7 wt% DMA-SO_3^- were named ZGE-3, ZGE-5, and ZGE-7. The content of each component in the precursor solution is shown in Table S1.†

Fig. S1a and b† present the ^{1}H NMR and ^{13}C NMR spectra of the zwitterionic crosslinker DMA-SO_3^-, and the chemical shifts of the different proton and carbon signals corresponded quite well with the spectra, indicating that DMA-SO_3^- was successfully synthesized. It can be seen from Fig. S2a† that the precursor solution (top image) got solidified after the photopolymerization (bottom image). The formation of the polymer gel confirmed that the polymerization reaction was successful. Fig. S2b† presents the photo images of the GFM (top image) and ZGE (bottom image). After the curing reaction, the film became translucent, proving that the zwitterion containing the polymer electrolyte was well integrated within the glass fiber skeleton. The FT-IR spectra of DMA-SO_3^-, VEC, PEGDMA, GE, and ZGE-5 are shown in Fig. 2a. The characteristic peak in the range of 1700–1850 cm^{-1} corresponded to the stretching vibration of –C=O.[36] It was noted that with incorporation of zwitterionic moieties in the polymer structure, –SO_3^- vibration peaks

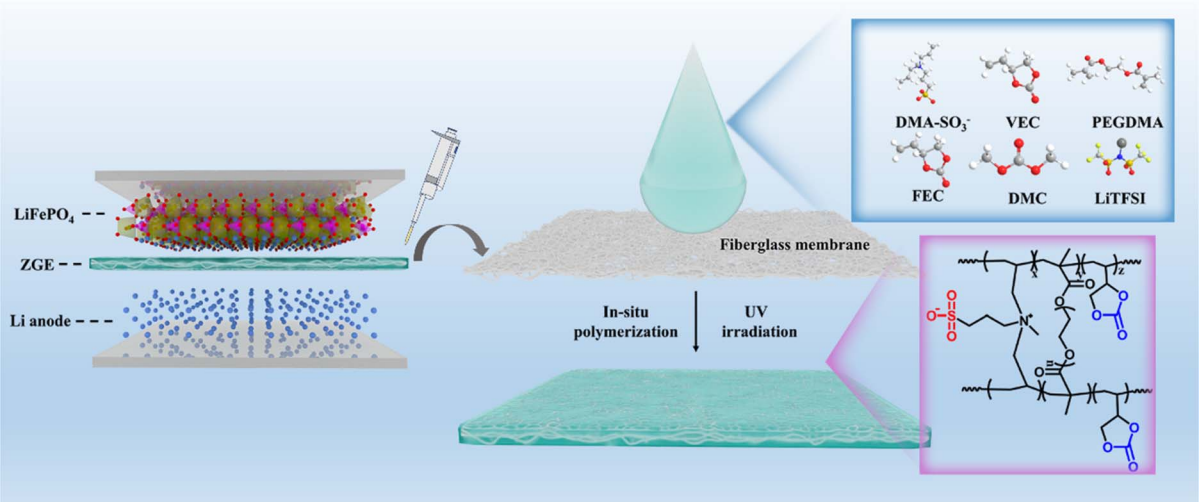

Fig. 1 Schematic diagram of the *in situ* preparation of the ZGE membrane.

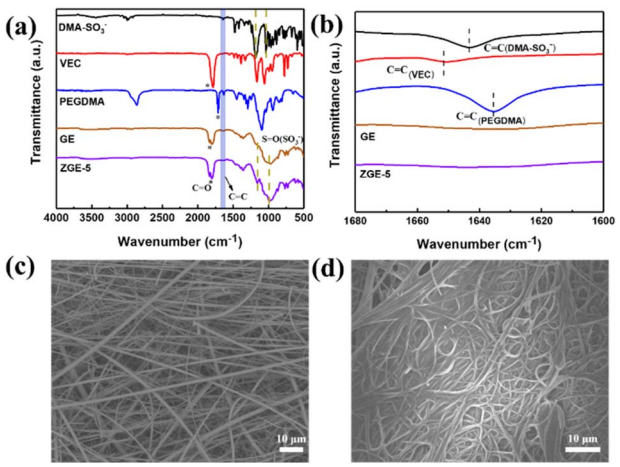

Fig. 2 (a) FT-IR spectra of DMA-SO_3^-, VEC, PEGDMA, GE, and ZGE-5; (b) zoomed-in FT-IR spectra of DMA-SO_3^-, VEC, PEGDMA, GE, and ZGE-5 in the wavenumber range of 1680–1600 cm^{-1}. SEM images of (c) GFM and (d) ZGE-5.

appeared at 1030 and 1151 cm^{-1}, as could be seen in the spectrum of ZGE-5.[37] In Fig. 2b, it can be seen that the C=C stretching vibrations of DMA-SO_3^-, VEC, and PEGDMA in the wavenumber range from 1600–1680 cm^{-1} disappeared, indicating a high conversion of the materials in the photopolymerization.[35]

As depicted in Fig. S3a,† the temperatures of GE, ZGE-3, -5, and -7 at a weight loss of 5% were about 100 °C, which resulted from the evaporation of DMC. As shown in Fig. S3b,† the tensile strength of ZGE-5 was 72 kPa, which was significantly higher than that of GFM (41 kPa). In addition, the Young's modulus of ZGE-5 (19.4 MPa) was more than seven times that of GE (2.52 MPa). The elongation at breaks of the two groups were similar. In Fig. 2c and d, the SEM images of GFM and ZGE are shown, and it can be seen that there are many voids in the GFM image, which allow the precursor solution to permeate. The diameter of a single glass fiber was about 5 μm. As for the ZGE, the polymer gel was evenly filled in the GFM, providing a continuous pathway for ion conduction.

2.2 Ion transport and electrochemical stability of ZGE

The relationship between σ and the temperature of ZGE was studied by AC impedance spectroscopy (Fig. 3a). The σ values of all the samples changed nonlinearly with temperature, and the

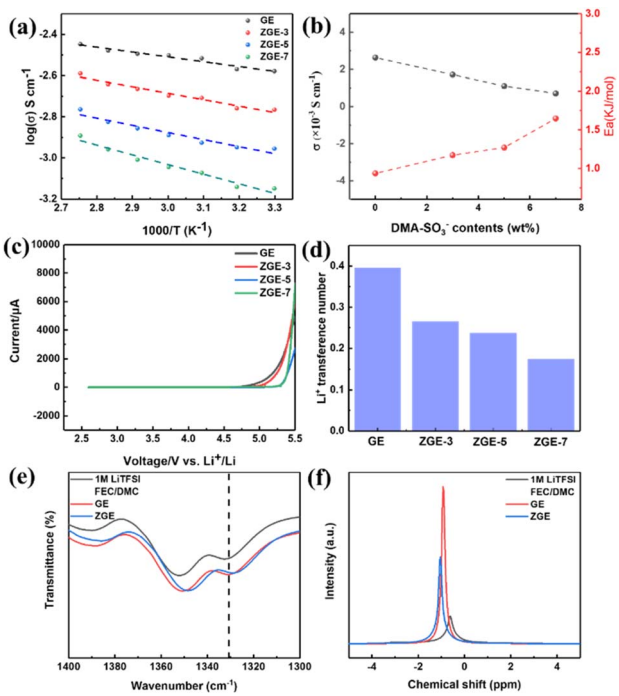

Fig. 3 (a) Variation of σ in ZGE-3, ZGE-5, ZGE-7, and GE as a function of temperature; (b) σ values at 30 °C and E_a fitted by VTF; (c) LSV curves and (d) t_{Li^+} values of ZGE-3, ZGE-5, and ZGE-7, and GE. (e) FT-IR spectra (wavenumber range of 1400–1300 cm^{-1}) and (f) ^{7}Li SSNMR spectra of ZGE, GE, and 1 M LiTFSI FEC/DMC.

temperature dependence of σ could be fitted by the Vogel–Tamman–Fulcher equation (VTF) equation:[38]

$$\sigma = AT^{-\frac{1}{2}}\exp\left[-\frac{E_a}{R(T-T_0)}\right] \quad (1)$$

where A refers to the pre-exponential factor, E_a is the activation energy, R is the ideal gas constant, and T_0 is the equilibrium glass transition temperature associated with T (also known as the Vogel temperature). At 30 °C, all the ZGE samples achieved high σ values, which were also satisfactory for polymer battery operation.[39] The σ values of ZGE-3, -5, and -7 were 1.71×10^{-3}, 1.15×10^{-3}, and 0.95×10^{-3} S cm^{-1}, respectively (Fig. 3b). The σ of GE (2.64×10^{-3} S cm^{-1}) was slightly larger than that of ZGE, which was possibly due to the fact that the polymer segments could easier move without the zwitterionic cross-linker. The electrochemical impedance spectroscopy (EIS) results for the electrolyte at 30 °C are shown in Fig. S4.† Fig. 3b shows the activation energy (E_a) obtained by VTF equation fitting. It can be seen that with the increase in zwitterion content, E_a also increased (from 0.94 kJ mol^{-1} to 1.65 kJ mol^{-1}), which may be caused by the strong zwitterion-ion interaction and as it was more difficult for the polymer chain segments to move.[40] The presence of polar zwitterions in ZGE promoted the dissociation of lithium salt (see Fig. 5a–d).[28,41] It was also interesting to find that as the proportion of the zwitterionic structure slightly increased within ZGE (from ZGE-3 to ZGE-7), σ gradually decreased. This was because DMA-SO_3^- had two double bonds in its molecular structure and could participate in polymer network formation during the curing reaction, so the crosslinking density increased as more DMA-SO_3^- was fed in to the precursor solution. Consequently, the segmental motion of the polymer matrix was restricted and ion transport slowed down to a certain degree.[42] Even so, σ was still quite high for ZGE-7 and almost at the level of 10^{-3} S cm^{-1}.

The electrochemical stability of the ZGE samples was studied by LSV. As shown in Fig. 3c, the oxidation potentials of ZGE-3, -5, -7, and GE were 4.9, 5.2, 5.2, and 4.6 V *vs.* Li^+/Li. It was possible that with the increase in zwitterion content, the crosslinking density increased, which means it would be more difficult for ZGE to decompose.[43] The cationic (Li^+) transference numbers (t_{Li^+}) of the ZGE samples are shown in Fig. 3d. Fig. S5† shows the chronoamperometry curves and AC impedance spectra of the Li/ZGE/Li cell before and after polarization. According to the Bruce–Vincent–Evans equation, the t_{Li^+} values of ZGE-3, -5, and -7 were calculated to be 0.27, 0.24, and 0.17. The t_{Li^+} of GE was 0.4. The high t_{Li^+} in GE could be attributed to the fact that more Li^+ was decoupled from the polymer chain and solvated by other electrolyte components.[18] The zwitterion in the polymer structure led to the decrease in t_{Li^+}, which might be due to the interaction between the zwitterion and Li^+, which further led to an increase in resistance to Li^+ motion.[30,44]

The ion complexation state in ZGE, GE, and the liquid electrolyte was analyzed. In the FT-IR spectra, the vibrational peak of FT-IR near 1330 cm^{-1} was assigned to the –SO_2 group of $TFSI^-$ (Fig. 3e).[38] In ZGE, this peak was obviously red-shifted in comparison with the same peak for the liquid electrolyte and the GE group, possibly due to the interaction between the zwitterions and $TFSI^-$. The coupling environment of Li^+ was further analyzed by ^{7}Li NMR (Fig. 3f). The chemical shift of ^{7}Li for the liquid electrolyte group was −0.63 ppm, while the resonance of ^{7}Li in the ZGE group was located at −1.05 ppm, which was also close to that of the GE group. The ^{7}Li NMR peak difference (about 0.42 ppm) between ZGE and the liquid electrolyte suggested that Li^+ in ZGE could possibly be coordinated with C=O, C–O–C, and –SO_3^- of the polymer besides the carbonates. The above results showed that ZGE had a high σ, which was contributed by the unique molecular structure and the additives. Subsequently, ZGE-5 was selected for further electrochemical characterization due to its suitable ionic conductivity, oxidation decomposition voltage, and t_{Li^+}.

2.3 Interfacial stability of ZGE with the Li metal anode

ZGE-5 and GE samples were assembled into a Li symmetrical cell to study the electrolytes' ability to suppress lithium dendrite growth. Fig. 4a shows the voltage response of the as-assembled Li/GE/Li cell at 30 °C when the current density was 0.1 mA cm^{-2} and the cycling capacity was 0.1 mA h cm^{-2}. The initial overpotential was about 25 mV (Fig. 4b). The occurrence of an internal short circuit was observed after cycling for 630 h. However, under the same conditions, the initial overpotential of the Li/Li cell containing ZGE-5 was 20 mV, which was lower than that of the Li/GE/Li group (as shown in Fig. 4e). Also, the cell could cycle stably without fluctuations or a sudden potential jump for over 1400 h. This performance was significantly superior to that of the Li/GE/Li cell. These results indicated that ZGE was obviously more advantageous than GE in promoting a stable SEI formation and inhibiting lithium dendrite growth. It was thought that the existence of the DMA-SO_3^- structure in ZGE not only helped regulate fast ion conduction but also promoted a benign SEI formation and uniform lithium deposition.

More experimental studies were performed to clarify the reason why ZGE had better electrolyte/lithium interfacial stability. Fig. S6a and b† show the Nyquist plots of Li/GE/Li and Li/ZGE-5/Li cells before and after 100 cycles of plating/stripping tests. After fitting the impedance results equivalent circuit (Fig. S6c†), the interfacial resistance of the Li/ZGE-5/Li cell before and after the cycles was 200 Ω and 230 Ω, respectively. ZGE-5 exhibited obviously lower interfacial impedance with regard to that of the Li/GE/Li cell (246 Ω). This result reflected that the SEI at the ZGE/lithium interface facilitated Li^+ migration and remained stable during cycling.

Fig. 5a–d show the Raman spectra for characterizing the association state of $TFSI^-$ in ZGE. The room temperature Raman spectra of ZGE-3, -5, -7, and GE in the Raman shift ranging from 700–750 cm^{-1} were fitted by the Gauss–Lorentz function. The S–N–S vibration peaks in the Raman spectrum could be deconvoluted into three separate peaks located at 727, 737, and 746 cm^{-1}, corresponding to the free $TFSI^-$, compact ion pair (CIP: the $TFSI^-$ was associated with one Li^+), and aggregated ion cluster (AGG: the $TFSI^{-1}$ was associated with more than two Li^+), respectively.[45] The percentage of free $TFSI^-$ was calculated as follows:

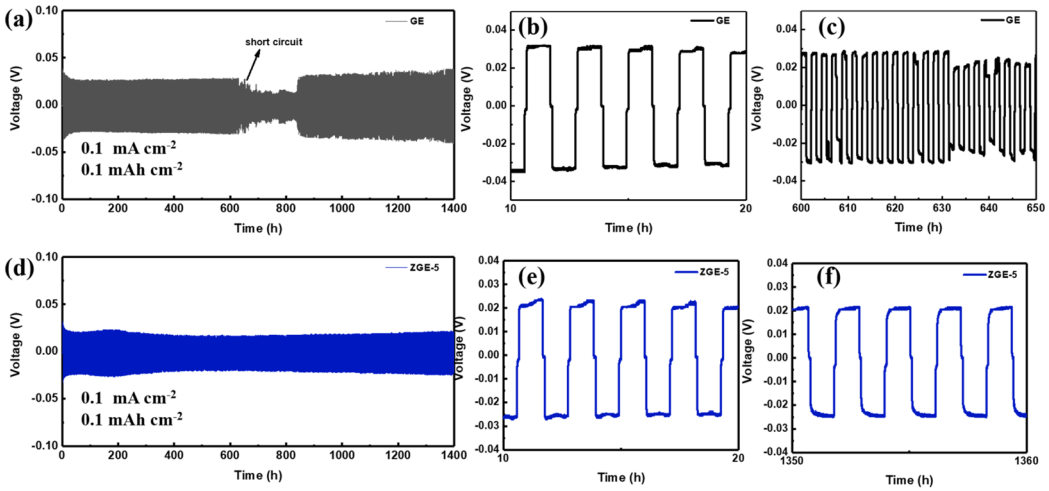

Fig. 4 (a) Constant current plating/stripping cycling curve and enlarged profile of the Li/GE/Li cell at (b) 10–20 h and (c) 600–650 h; (d) constant current plating/stripping cycling curve and enlarged profile of the Li/ZGE-5/Li cell at (e) 10–20 h and (f) 1350–1360 h.

$$\mathrm{TFSI}_{\mathrm{free}}^{-} = \frac{A(\mathrm{free})}{A(\mathrm{free}) + A(\mathrm{CIP}) + A(\mathrm{AGG})} \times 100\% \quad (2)$$

The percentages of free $TFSI^-$ in GE, ZGE-3, -5, and -7 were 36.8%, 39.3%, 44.5%, and 49.2%, respectively. With the increase in zwitterion content in the ZGE samples, the proportion of free $TFSI^-$ increased and more Li^+ was dissociated. More Li^+ was thus available to form solvated structures with FEC and DMC, which was beneficial for the reduction reaction to form the SEI.[46–48]

The Tafel curves (Fig. 5g) and extracted exchange current density values (Fig. 5j) of the Li/ZGE-5/Li and Li/GE/Li cells revealed that the Li/ZGE-5/Li cell had a slower surface reaction rate at the electrode, suggesting a better Li deposition stability.[20] The EDS mapping of ZGE-5 (Fig. S7†) proved the uniform distribution of S element, which also reflected the uniform distribution of $-SO_3^-$ in the zwitterionic structure. This was favorable for achieving a uniform deposition of Li^+. The SEM images of the lithium metal surface (retrieved from the Li/ZGE-5/Li cell after plating/stripping cycling for 20 h and 200 h in Fig. 4) are shown in Fig. 5h and i. As a control, Fig. 5e and f show the lithium metal surface (retrieved from the Li/GE/Li cell after the same cycling periods in Fig. 4). As expected, the Li foil from the Li/ZGE-5/Li cell had fewer protrusions and was smoother compared with that from the Li/GE/Li cell.

In addition, after the plating/stripping test shown in Fig. 4 for 100 cycles, the full spectra from XPS of the Li electrode surfaces harvested from the Li/ZGE-5/Li and Li/GE/Li cells are shown in Fig. S8,† and the corresponding contents of C, F, and O elements on the different Li electrode surfaces are shown in Fig. S8c.† As shown in Fig. 5k and *n*, the C 1s peaks at 284.5, 285.8, 287.8, and 292.6 eV belonged to C–C, C–O, O–C=O, and CO_3^{2-}, respectively, indicating that the SEI was composed of organic and inorganic compounds. In the F 1s spectra (Fig. 5l and o), the peak at 685.0 eV corresponded to LiF. It could thus be seen that the Li/ZGE-5/Li cell formed a LiF-rich SEI layer on the surface of Li. The LiF came from the reduction of LiTFSI and FEC.[49] The lithiophobic LiF has a high surface energy as well as shear modulus, which can guide the Li to deposit along the interface of Li/SEI and effectively inhibit the growth of lithium dendrites.[24,50] In the O 1s spectra (Fig. 5m and p), the peak at 531.7 eV corresponded to C–O–C, indicating that the SEI layer formed by ZGE-5 was rich in C–O–C components. Ether bonds containing organic compounds in the SEI can promote the transport of Li^+ within the SEI, thereby reducing the interfacial impedance,[51] which was also the reason for the low interfacial impedance of the Li/ZGE-5/Li cell after 100 plating/stripping cycles, as was discussed above.

The Li/GE/Li and Li/ZGE-5/Li cells were simulated by using a finite element method using COMSOL Multiphysics to aid understanding the mechanism of Li^+ flux on the lithium metal through the different electrolytes (Fig. 6a–f). Prior to deposition, some protrusions inevitably formed on the lithium electrode. The protruding area region showed a stronger electric field, and Li^+ was deposited around the tip (Fig. 6b). This often leads to the formation of lithium dendrites.[52] When the steady state was reached in the deposition process, the ZGE-contacted Li had an obviously smaller current density and electric field strength than that of the GE-contacted Li at the protrusions. In the concave area, the ZGE-contacted Li had a larger current density and electric field strength than that of the GE-contacted Li. These indicate that the Li deposition was more uniform in the Li/ZGE/Li cell, which was due to the electrostatic shielding effect brought by the cations in the zwitterions of ZGE.[53] Moreover, the anions in the zwitterions of ZGE could also guide the uniform distribution of Li^+.[31,54] As shown in Fig. 6c and f, the interfacial area of ZGE/Li showed a more uniform distribution Li^+ concentration,[52] which was about 0.4 mol L^{-1} in both the concave and convex places. Overall, the COMSOL simulation demonstrated that ZGE could promote a more homogeneous and stable Li^+ flux.

The deposition process of lithium and the formation of the SEI can be explained as follows (Fig. 7). In short, the protrusion area on the surface of lithium metal has a higher electric field

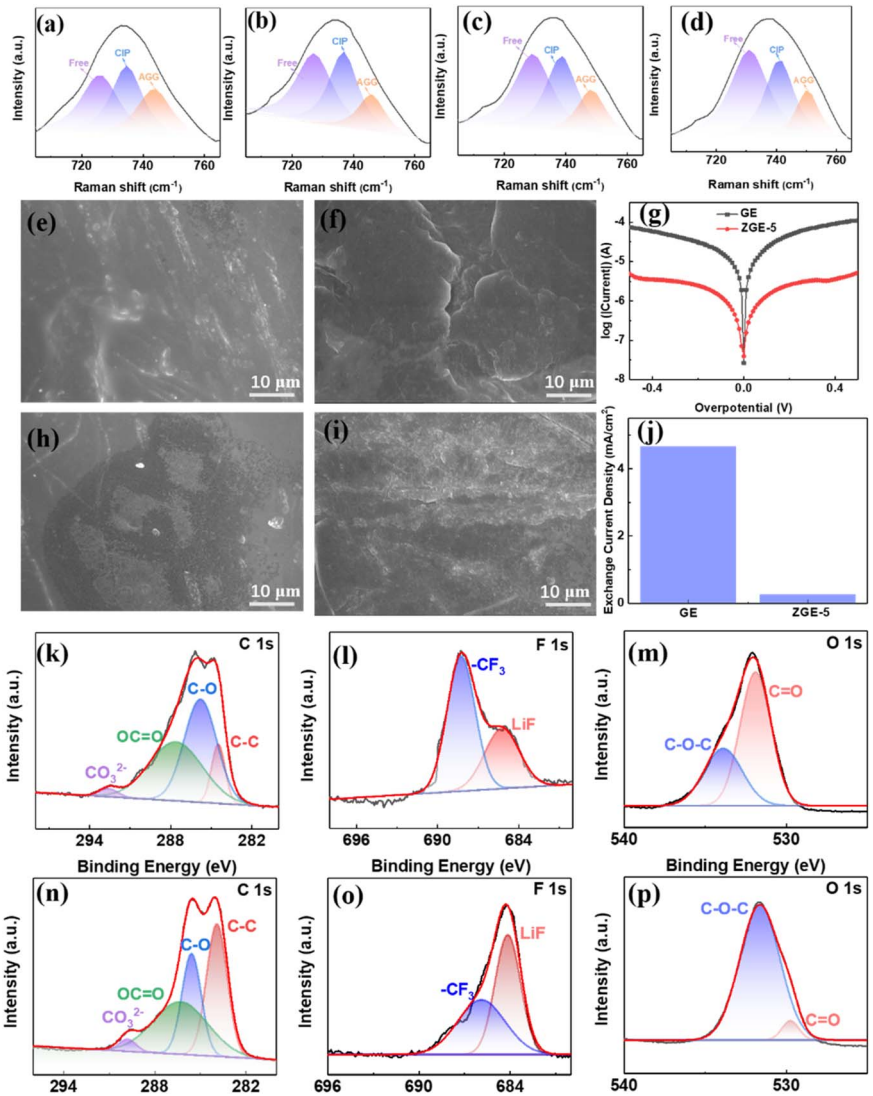

Fig. 5 Raman spectra of (a) GE, (b) ZGE-3, (c) ZGE-5, and (d) ZGE-7. SEM images of the lithium metal surface at (e) 20 h and (f) 200 h during the cycling process of the Li/GE/Li cell; SEM images of the lithium metal surface at (h) 20 h and (j) 200 h during the cycling process of the Li/ZGE-5/Li cell. (g) Tafel plots of GE and ZGE-5 obtained from voltammetry measurements performed at a scan rate of 10 mV s; (i) extracted exchange current density values from the Tafel plots. XPS spectra of (k) C 1s, (l) F 1s, and (m) O 1s on the surface of lithium metal during the cycling process of the Li/GE/Li cell after 100 cycles; XPS spectra of (n) C 1s, (o) F 1s, and (p) O 1s on the surface of lithium metal during the cycling process of the Li/ZGE-5/Li cell after 100 cycles.

strength at the beginning of plating. Li^+ preferentially deposits at the tip, resulting in a continuous growth of lithium dendrites. The electrostatic shielding effect induced by cations in the zwitterions in ZGE homogenizes the current and electric field strength distribution. Moreover, the $-SO_3^-$ in the zwitterions of ZGE guides the uniform distribution of Li^+, resulting in a uniform deposition of Li^+, and a flat Li surface formation. In addition, the zwitterions dissociate more Li^+ from LiTFSI,[54] and more Li^+ are available to form a solvated sheath structure with FEC and DMC. As it breaks down, an SEI structure rich in LiF and C–O–C is formed.

2.4 Full cell performance of ZGE

The performance of the Li/LFP cell with the ZGE-5 electrolyte was evaluated. Fig. 8a shows the CV curves of the Li/ZGE-5/LFP cell. The peaks observed at 3.61 V *vs.* Li^+/Li and 3.24 V *vs.* Li^+/Li corresponded to the process of Li deposition and stripping in the LFP electrode.[55,56] The first and second CV curves did not coincide, which was due to the formation of the SEI. The subsequent curve almost overlapped with the curve of the second cycle, indicating a good redox reversibility. Fig. 8b shows the rate performances of the Li/ZGE-5/LFP cells at current densities ranging from 0.1C to 5C. At 0.1C, 0.2C, 0.3C, 0.5C, 1C, 2C, 3C, 4C, and 5C, the discharge capacities of the Li/ZGE-5/LFP cell were 165, 164, 163, 161, 154, 140, 127, 105, and 79 mA h g^{-1}, respectively. Even at 5C, the discharge capacity was still as high as 79 mA h g^{-1}. When the current density was restored to 0.1C, the discharge capacity returned to 165 mA h g^{-1}, showing an excellent rate capability.

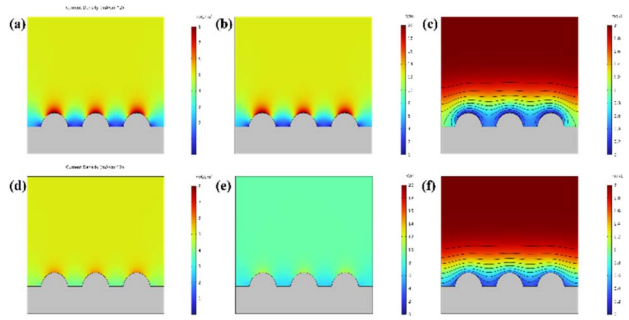

Fig. 6 COMSOL simulations of the plating process on the lithium electrode of Li/GE/Li and Li/ZGE-5/Li cells (the upper layer is the electrolyte, the lower layer is lithium metal). The plots of current density distribution in the cells with (a) GE and (d) ZGE-5 electrolytes when the plating process reached a steady state; the distribution of electric field strengths in the cells with (b) GE and (e) ZGE-5 electrolytes; the distribution of Li^+ concentrations of the cells with (c) GE and (f) ZGE-5 electrolytes.

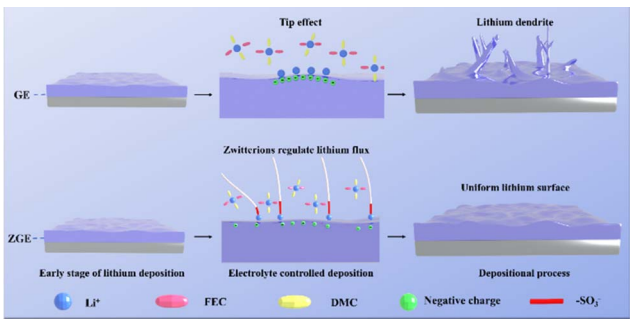

Fig. 7 Schematic diagram of the deposition of Li^+ on lithium electrodes through GE and ZGE-5 electrolytes.

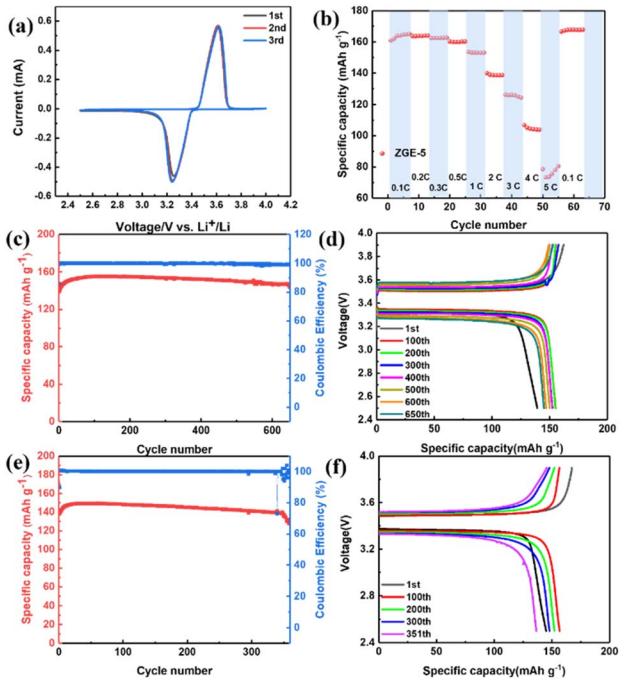

Fig. 8 (a) CV curve of the Li/ZGE-5/LFP cell at a scanning rate of 0.1 mV s^{-1}; (b) rate performance of the Li/ZGE-5/LFP cell; (c) cycling performance of the Li/ZGE-5/LFP cell at 1C; (d) charge and discharge curves of the Li/ZGE-5/LFP cell in different cycles at 1C; (e) cycling performance of the Li/GE/LFP cell at 1C; (f) charge and discharge curves of the Li/GE/LFP cell in different cycles at 1C (CV, rate performance tests, and cycling performance tests were all conducted at 30 °C).

Fig. 8c shows the cycling performance of the Li/ZGE-5/LFP cell at 1C. The initial discharge capacity was 141 mA h g^{-1}, which gradually stabilized at 155 mA h g^{-1}. After 600 cycles, the discharge capacity still retained 143 mA h g^{-1}, while the capacity retention reached 92%, and the coulombic efficiency was >99.5%. Fig. 8d shows the charge and discharge curves of the Li/ZGE-5/LFP cells at different cycles. No significant increase in ohmic polarization was observed from the charge–discharge curves even after 600 cycles. The cycling performance of the Li/GE/LFP cell at 1C is shown in Fig. 8c, where the initial discharge capacity of the battery was 140 mA h g^{-1}, and the coulombic efficiency was 95.3%. After 20 cycles, the discharge capacity gradually stabilized at 150 mA h g^{-1}. However, after 350 cycles, the discharge capacity gradually decreased, and a short circuit occurred. This was probably due to the non-uniform lithium deposition, which caused the lithium dendrites to grow rapidly until they eventually pierced the electrolyte membrane. It was also noted that the number of stable cycles of the Li/ZGE-5/LFP cell was almost twice that of the Li/GE/LFP cell under the same cycling conditions. This significantly enhanced performance was contributed by the uniform lithium deposition and LiF-rich SEI in the Li/ZGE-5/LFP cell. Fig. S9† also shows the performances of the Li/ZGE-5/LFP cell at high rates (2C and 3C). It could be seen that the Li/ZGE-5/LFP cell had a high initial discharge capacity at high rates (132 mA h g^{-1} at 2C and 124 mA h g^{-1} at 3C). Moreover, the Li/ZGE-5/LFP cell was stable without short circuiting at 650 cycles under 2C and remained relatively stable at 350 cycles under 3C.

Li/ZGE-5/NCA cells were also assembled for performance evaluation. The results are shown in Fig. 9. At 0.2C and 30 °C, the initial discharge capacity of the Li/ZGE-5/NCA cell was 232 mA h g^{-1}. After 100 cycles, the discharge capacity was 164 mA h g^{-1} (Fig. 9a). In contrast, the initial discharge capacity of the Li/GE/NCA cell was slightly lower (225 mA h g^{-1}), and the discharge capacity decreased to only 89 mA h g^{-1} after 100 cycles (Fig. 9b). The discharge capacity of the Li/ZGE-5/NCA cell was twice of that of the Li/GE/NCA cell at the 150th cycle (Fig. 9d and e), contributed by the more stable lithium deposition behavior, which reduced the occurrence of interface side reactions.[57] Moreover, the presence of zwitterions might make the cathode/electrolyte interphase more effective in passivating the active cathode surface.[58] These results suggest that ZGE exhibited good electrochemical stability in 4 V class LMBs. A Li/ZGE/LFP flexible pouch cell was further prepared. The cell could power an LED normally in the flat state (Fig. 9g) and under a 180° bending state (Fig. 9h), demonstrating its superior mechanical robustness and good safety. It is worth mentioning that the flexible battery could continuously charge and discharge, with an energy density of 89.4 W h kg^{-1} (Fig. 9c),

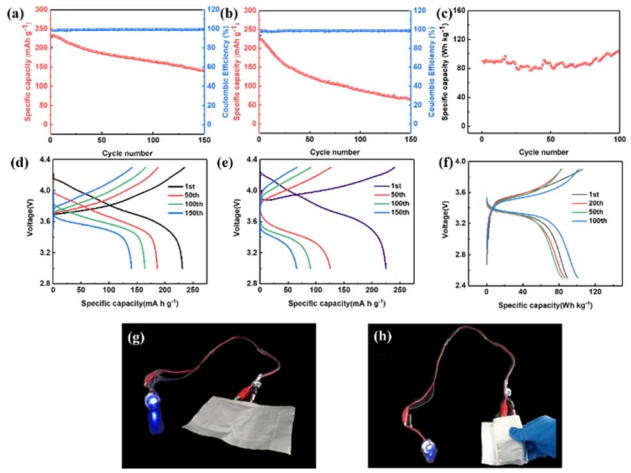

Fig. 9 Cycling performance of the (a) Li/ZGE-5/NCA cell and (b) Li/GE/NCA cell at 0.2C; charge and discharge curves of the (d) Li/ZGE-5/NCA cell and (e) Li/GE/NCA cell at different cycles. (c) Cycling performance and (f) charge and discharge curves of the Li/ZGE-5/LFP pouch cell at 0.2C (the above battery performance tests were all conducted at 30 °C); photographs of the Li/ZGE-5/LFP pouch cell to light up LED lights (g) before and (h) after folding.

indicating that it has broad application prospects in the field of flexible/wearable devices.

3. Conclusions

To sum up, starting from macromolecular structural design and synthesis, we successfully developed a zwitterionic-crosslinker-incorporated polymer electrolyte network, and the ultimate electrolyte sample ZGE could be prepared *in situ*. ZGE exhibited a high room temperature conductivity value ($>1 \times 10^{-3}$ S cm^{-1}) and a wide electrochemical stability window. The zwitterionic crosslinker not only promoted the homogeneous deposition of Li^+ flux and inhibited lithium dendrite growth, but on the anode it also helped increase the fraction of LiF within the SEI obviously. For example, in the plating/stripping tests, the Li/Li cell with the ZGE sample could cycle stably for over 1400 h with a current density of 0.1 mA cm^{-2}. Afterwards, the Li/ZGE/LFP that was prepared *in situ* was able to cycle stably with a high capacity retention of 92% after 600 cycles at 1C (155 mA h g^{-1} to 143 mA h g^{-1}). Besides, ZGE also enabled a Li/NCA cell to charge and discharge with a high specific capacity (232 mA h g^{-1}). Finally, the potential application of ZGE in a flexible pouch cell was realized. This research work demonstrates a promising way to develop flexible polymer electrolytes that could simultaneously regulate ion transport, and deposition, as well as SEI optimization for realizing next-generation high-performance solid-state LMBs.

4. Experimental methods

4.1 Materials

Diallylmethylamine (DMA, 98%, Aladdin), 1,3-propane sultone (98%, Aladdin), vinyl ethylene carbonate (VEC, 99%, Aladdin), poly(ethylene glycol) dimethacrylate (PEGDMA, Aladdin, M_n = 750), dimethyl carbonate (DMC, 98%, Sigma-Aldrich), fluoroethylene carbonate (FEC, 98%, Aladdin), bis(trifluoromethane) sulfonimide lithium salt (LiTFSI, 99%, Aladdin), 2-hydroxy-2-methylpropiophenone (HMPP, 97%, Aladdin), acetonitrile (ACN, 99.9%, Adamas), diethyl ether (DEE, AR), lithium iron phosphate ($LiFePO_4$, Sud-Chemie, theoretical specific capacity: 170 mA h g^{-1}), $LiNi_{0.815}Co_{0.15}Al_{0.035}O_2$ (NCA, theoretical specific capacity: 278 mA h g^{-1}), glass microfiber filters (Whatman Grade GF/A), polyvinylidenefluoride (PVDF, MTI, M_n = 600 kDa), Super-P (MTI), and *N*-methyl-2-pyrrolidone (NMP, 99.5%, Aladdin) were purchased without further purification. Lithium electrodes (thickness = 50 μm, r = 0.78 cm) and lithium metal strips (thickness = 100 μm) were purchased from China Energy Lithium Co., Ltd.

4.2 Preparation of the zwitterionic crosslinker 3-(*N*,*N*-diallyl-*N*-methylammonium) propanesulfonate (DMA-SO_3^-)

DMA-SO_3^- was synthesized according to a literature reported method. First, a three-necked flask was purged with N_2 for 20 min to remove water and air from the flask, and then 1,3-propane sultone (0.1 mol) was dissolved in 40 ml ACN and added to the flask. DMA (0.09 mol) was added and stirred at room temperature for 6 h. During this time, the product formed a white precipitate. The sediment was then filtered and washed three times with 40 mL DEE. Finally, the sample was vacuum-dried at 30 °C for 8 h. The crosslinker yield was 78%. ^{1}H NMR (400 MHz, D_2O): δ 6.03 (ddt, J = 17.4, 10.3, 7.4 Hz, 2H, CH_2 = C*H*CH$_2$N, N CH$_2$C*H* = CH$_2$), 5.78–5.57 (m, 4H, C*H*$_2$ = CHCH$_2$N, NCH$_2$CH = C*H*$_2$), 4.02–3.84 (m, 4H, CH$_2$ = CHC*H*$_2$N, NC*H*$_2$CH = CH$_2$), 3.48–3.34 (m, 2H, NC*H*$_2$CH$_2$CH$_2$S), 3.02 (s, 3H, N–C*H*$_3$), 2.96 (t, J = 7.2 Hz, 2H, NCH$_2$CH$_2$C*H*$_2$S), 2.32–2.16 (m, 2H, NCH$_2$C*H*$_2$CH$_2$S). ^{13}C NMR (101 MHz, D_2O): δ 129.04 (*C*H$_2$-CHCH$_2$N, NCH$_2$CH*C*H$_2$), 123.99 (CH$_2$*C*HCH$_2$N, NCH$_2$*C*HCH$_2$), 63.85 (CH$_2$CH*C*H$_2$N, N*C*H$_2$CHCH$_2$), 59.10 (N*C*H$_2$CH$_2$CH$_2$S), 47.15 (NCH$_2$CH$_2$*C*H$_2$S, N–*C*H$_3$), 17.77 (NCH$_2$*C*H$_2$CH$_2$S).

4.3 Preparation of the zwitterionic gel electrolyte (ZGE)

First, a Whatman glass fiber membrane was placed in a vacuum oven at 60 °C for 12 h to remove the adsorbed water. The dried glass fiber membrane was then cut into 16 mm diameter disks, which were then stored in a glovebox filled with argon gas before use. The preparation process of ZGE-5 is shown in Fig. 1. First, 5 wt% DMA-SO_3^-, 16 wt% VEC, 2 wt% PEGDMA and 2 wt% HMPP were weighed and added to 75 wt% 1 M LiTFSI FEC/DMC (1 : 4 v/v) solution in a glove box filled with argon gas. The components were allowed to dissolve to form a transparent solution. Then the solution was dropped into the glass fiber membrane, and the whole was illuminated by ultraviolet light for free radical polymerization. Finally, electrolytes containing non-*in situ* zwitterionic polymers were obtained. The ZGE could be *in situ* formed on the surface of the lithium anode before battery assembly. For example, the glass fiber membrane was covered on the surface of the lithium anode, and then the precursor solution was dropped into the membrane, and next the reactants were polymerized under ultraviolet light for 15 min. The λ of the UV lamp used was 365 nm and the power

was 100 W. After that, the cell was further assembled. The electrolytes that did not contain DMA-SO_3^- were named GE, and the electrolytes that contained 3 wt% DMA-SO_3^-, 5 wt% DMA-SO_3^-, and 7 wt% DMA-SO_3^- were named ZGE-3, ZGE-5, and ZGE-7, respectively. The content of each component is shown in Table S1.†

4.4 Characterization

Liquid nuclear magnetic resonance (NMR) patterns were measured using a Bruker Avance NEO 400 MHz instrument. Fourier transform infrared (FT-IR) spectra were recorded on a Thermo Fisher Nicolet Is10 spectrometer. Raman spectra were recorded on a confocal Raman spectrometer (Thermo Fisher, Dxi) equipped with an FRA 106 Raman module, with the 1064 nm line of a Nd:YAG laser used as the excitation source (laser wavelength = 532 nm). The laser power was set to 250 mW and the spectral resolution was <2 cm^{-1}. Thermogravimetric analysis (TGA) measurements were performed on an STA 449 F3 Jupiter simultaneous thermal analyzer at a heating rate of 10 K min^{-1} under a N_2 atmosphere from 30 °C to 800 °C. Field emission scanning electron microscopy (FESEM, thermo scientific Apreo 2C) was used to study the surface morphology, while the corresponding EDS mappings were performed on an FEI Talos F200X instrument. The JNM-ECZ600R NMR spectrometer was used to test the 7Li solid-state magnetic resonance. The rotor diameter was 3.2 mm, the experimental method was single pulse, the relaxation time was 5 s, the sampling frequency was 16, and the linewidth factor was 20 Hz. The chemical shift of ^7Li refers to 0.1 M LiCl solution at 0 ppm. X-Ray photoelectron spectroscopy (XPS) was performed on a Thermo Scientific K-Alpha$^+$ instrument. During the measurement, the vacuum degree of the vacuum chamber was 5 $\times 10^{-9}$ mba. The X-ray source used was a monochromatic Al Kα source ($h\nu$ = 1486.6 eV). The working voltage was 15 kV. The filament current was 15 mA. The analyzer scan mode was CAE. During the experiment, the sample was protected by argon. The tensile properties were measured on a tensile tester (ZQ-990B-200, ZHIQU Precision Instrument Co. Ltd., China) with a tensile rate of 5 mm min^{-1}. GE and ZGE-5 were processed into dumbbell-shaped samples (12 mm × 2 mm × 0.20 mm, length × width × thickness) and tested.

4.5 Electrochemical measurements

The ionic conductivity (σ) was detected by electrochemical impedance spectroscopy (EIS) in the frequency range from 0.1 Hz to 1 MHz with a 10 mV alternating current input signal. Also, σ was calculated based on the equation:

$$\sigma = \frac{L}{RS} \tag{3}$$

where R is the resistance value of the SS/SS cells (the intercept on the x-axis in EIS results), and L and S are the thickness and area of the ZGE.

The lithium ion transference number (t_{Li^+}) was measured by a combined DC polarization and AC impedance method. Here, t_{Li^+} was calculated according to the equation:

$$t_{Li^+} = \frac{I_s(\Delta V - I_0 R_0)}{I_0(\Delta V - I_s R_s)} \tag{4}$$

where ΔV is the applied voltage (10 mV), I_0 and I_S are the initial and steady current through the cell, respectively, and R_0 and R_S are the initial and steady resistance.

Linear sweep voltammetry (LSV) was completed with Li/SS cells at a scan rate of 1 mV s^{-1} in the potential range of 2.0–6.0 V *vs.* Li^+/Li at 30 °C. Cyclic voltammetry (CV) testing was performed with a scan rate of 0.1 mV s^{-1} over 2.5–4.0 V *vs.* Li^+/Li for the Li/LFP cell at 30 °C. The above electrochemical tests were completed on an IVIUM Vertex C EIS electrochemical workstation (Netherlands). The plating/stripping tests of symmetrical Li/Li cells were completed using the LANHE CT2001A battery test system at 30 °C and at different current densities for 1 h plating and 1 h stripping, respectively. To prepare the LFP cathode, LFP slurry was prepared by mixing 80 wt% LFP, 10 wt% PVDF, and 10 wt% Super-P in anhydrous NMP. The slurry was spread on aluminum foil by a doctor blade. The cathode was dried in a vacuum oven at 80 °C for 8 h. The LFP cathode sheet (mass load 1.6 mg cm^{-2}) was cut into 12 mm diameter disks and placed in an argon-filled glove box (H_2O and O_2 content <0.1 ppm). The preparation method for the NCA cathode was the same as that for LFP, and the mass loading was 1.5 mg cm^{-2}. The pouch cell was 4 × 4 cm in size. The mass loading of the $LiFePO_4$ cathode was 2.2 mg cm^{-2}. Also, the N/P of the pouch cell was 356.39. The test voltage of the Li/LFP coin cell and pouch cell at 30 °C was 2.5–3.9 V. The test voltage of the Li/NCA cell at 30 °C was 3–4.3 V.

4.6 Finite element method simulation details

COMSOL Multiphysics software was used for the finite element simulation, and the zwitterionic gel electrolyte was taken as an example to set the specific parameters. The geometry was set as follows: the size of the half-cell model was a rectangle of 50 × 100 μm, the thickness of the metal lithium anode was 10 μm, the height of each lithium spike was 3 μm, and the width was 2 μm. The initial concentration of the electrolyte Li^+ was 2.99 mol cm^{-3}, and the conductivity was 2.09 × 10^{-3} S cm^{-1}. The diffusion coefficient was 3.21 × 10^{-10} cm^2 s^{-1} and the boundary current density was 0.1 mA cm^{-2}. The current density in the electrolyte was 1 mA cm^{-2} and the Li^+ concentration was 1 M.

Data availability

Data available on request: the data underlying this article will be shared on reasonable request to the corresponding author.

Author contributions

L. C.: data curation, investigation, formal analysis, resources, writing – original draft. Z. Z.: methodology, investigation, resources. Z. Y.: methodology, resources. G. Y.: conceptualization, funding acquisition, methodology, project administration, resources, supervision, writing – review & editing.

Conflicts of interest

The authors declare that they have no known competing financial interests or personal relationships that could have appeared to influence the work reported in this paper.

Acknowledgements

The research was financially supported by National Natural Science Foundation of China (No. 52021001, 51903030), Sichuan Provincial Science and Technology Department (No. 99203070), and Open Project of National Engineering Research Center of Electromagnetic Radiation Control Materials of University of Electronic Science and Technology of China (No. KPKFJJ2023004-2).

References

1 J. Xu, J. Zhang, T. P. Pollard, Q. Li, S. Tan, S. Hou, H. Wan, F. Chen, H. He, E. Hu, K. Xu, X.-Q. Yang, O. Borodin and C. Wang, Electrolyte design for Li-ion batteries under extreme operating conditions, *Nature*, 2023, **614**, 694–700.

2 Z. Li, J. Fu, X. Zhou, S. Gui, L. Wei, H. Yang, H. Li and X. Guo, Ionic Conduction in Polymer-Based Solid Electrolytes, *Adv. Sci.*, 2023, **10**, 2201718.

3 M. S. Kim, Z. Zhang, P. E. Rudnicki, Z. Yu, J. Wang, H. Wang, S. T. Oyakhire, Y. Chen, S. C. Kim, W. Zhang, D. T. Boyle, X. Kong, R. Xu, Z. Huang, W. Huang, S. F. Bent, L.-W. Wang, J. Qin, Z. Bao and Y. Cui, Suspension electrolyte with modified Li^+ solvation environment for lithium metal batteries, *Nat. Mater.*, 2022, **21**, 445–454.

4 Q. Wang, H. Wang, J. Wu, M. Zhou, W. Liu and H. Zhou, Advanced electrolyte design for stable lithium metal anode: From liquid to solid, *Nano Energy*, 2021, **80**, 105516.

5 J. Fu, Z. Li, X. Zhou, Z. Li and X. Guo, Fluorinated Solid Electrolyte Interphase Derived From Fluorinated Polymer Electrolyte To Stabilize Li Metal, *ChemSusChem*, 2023, **16**, e202300038.

6 Q. Wang, P. Zou, L. Ren, S. Wang, Y. Wang, Z. Huang, Z. Hou, Z. Jiang, X. Lu, T. Lu, L. Guan, L. Hou, C. Yang, W. Liu and Y. Wei, Ultrathin Composite Li Electrode for High-Performance Li Metal Batteries: A Review from Synthetic Chemistry, *Adv. Funct. Mater.*, 2023, **33**, 2213648.

7 X. Hu, Y. Gao, B. Zhang, L. Shi and Q. Li, Superior cycle performance of Li metal electrode with {110} surface texturing, *EcoMat*, 2022, **4**, e12264.

8 X. Hu, Y. Gao, Y. Sun, Z. Hou, Y. Luo, D. Wang, J. Wang, B. Zhang, Z. Zheng and Q. Li, Preserving the Li {110} Texture to Achieve Long Cycle Life in Li Metal Electrode at High Rates, *Adv. Funct. Mater.*, 2024, **34**, 2307404.

9 S. Zhang, S. Xiao, D. Li, J. Liao, F. Ji, H. Liu and L. Ci, Commercial carbon cloth: An emerging substrate for practical lithium metal batteries, *Energy Storage Mater.*, 2022, **48**, 172–190.

10 C. Z. Zhao, H. Duan, J. Q. Huang, J. Zhang, Q. Zhang, Y. G. Guo and L. J. Wan, Designing solid-state interfaces on lithium-metal anodes: a review, *Sci. China Chem.*, 2019, **62**, 1286–1299.

11 S. Zhang, R. Li, N. Hu, T. Deng, S. Weng, Z. Wu, D. Lu, H. Zhang, J. Zhang, X. Wang, L. Chen, L. Fan and X. Fan, Tackling realistic Li^+ flux for high-energy lithium metal batteries, *Nat. Commun.*, 2022, **13**, 5431.

12 Z. Song, F. Chen, M. Martinez-Ibañez, W. Feng, M. Forsyth, Z. Zhou, M. Armand and H. Zhang, A reflection on polymer electrolytes for solid-state lithium metal batteries, *Nat. Commun.*, 2023, **14**, 4884.

13 S. Randau, D. A. Weber, O. Kötz, R. Koerver, P. Braun, A. Weber, E. Ivers-Tiffée, T. Adermann, J. Kulisch, W. G. Zeier, F. H. Richter and J. Janek, Benchmarking the performance of all-solid-state lithium batteries, *Nat. Energy*, 2020, **5**, 259–270.

14 D. E. Fenton, J. M. Parker and P. V. Wright, Complexes of alkali metal ions with poly(ethylene oxide), *Polymer*, 1973, **14**, 589.

15 B. Guo, Y. Fu, J. Wang, Y. Gong, Y. Zhao, K. Yang, S. Zhou, L. Liu, S. Yang, X. Liu and F. Pan, Strategies and characterization methods for achieving high performance PEO-based solid-state lithium-ion batteries, *Chem. Commun.*, 2022, **58**, 8182–8193.

16 H. Wang, L. Sheng, G. Yasin, L. Wang, H. Xu and X. He, Reviewing the current status and development of polymer electrolytes for solid-state lithium batteries, *Energy Storage Mater.*, 2020, **33**, 188–215.

17 X. Yu and A. Manthiram, Electrode–electrolyte interfaces in lithium-based batteries, *Energy Environ. Sci.*, 2018, **11**, 527–543.

18 G. Yang, Y. Song, Q. Wang, L. Zhang and L. Deng, Review of ionic liquids containing, polymer/inorganic hybrid electrolytes for lithium metal batteries, *Mater. Des.*, 2020, **190**, 108563.

19 G. Xi, M. Xiao, S. Wang, D. Han, Y. Li and Y. Meng, Polymer-Based Solid Electrolytes: Material Selection, Design, and Application, *Adv. Funct. Mater.*, 2021, **31**, 2007598.

20 J. Li, T. Zhang, X. Hui, R. Zhu, Q. Sun, X. Li and L. Yin, Competitive Li^+ Coordination in Ionogel Electrolytes for Enhanced Li-Ion Transport Kinetics, *Adv. Sci.*, 2023, **10**(23), 2300226.

21 L. Tang, B. Chen, Z. Zhang, C. Ma, J. Chen, Y. Huang, F. Zhang, Q. Dong, G. Xue, D. Chen, C. Hu, S. Li, Z. Liu, Y. Shen, Q. Chen and L. Chen, Polyfluorinated crosslinker-based solid polymer electrolytes for long-cycling 4.5 V lithium metal batteries, *Nat. Commun.*, 2023, **14**, 2301.

22 X. Xie, P. Zhang, X. Li, Z. Wang, X. Qin, M. Shao, L. Zhang and W. Zhou, Rational Design of F-Modified Polyester Electrolytes for Sustainable All-Solid-State Lithium Metal Batteries, *J. Am. Chem. Soc.*, 2024, **146**, 5940–5951.

23 Q. Sun, S. Wang, Y. Ma, D. Song, H. Zhang, X. Shi, N. Zhang and L. Zhang, Li-Ion Transfer Mechanism of Gel Polymer Electrolyte with Sole Fluoroethylene Carbonate Solvent, *Adv. Mater.*, 2023, **35**, 2300998.

24 W. Zhang, V. Koverga, S. Liu, J. Zhou, J. Wang, P. Bai, S. Tan, N. K. Dandu, Z. Wang, F. Chen, J. Xia, H. Wan, X. Zhang, H. Yang, B. L. Lucht, A.-M. Li, X.-Q. Yang, E. Hu,

S. R. Raghavan, A. T. Ngo and C. Wang, Single-phase local-high-concentration solid polymer electrolytes for lithium-metal batteries, *Nat. Energy*, 2024, **9**(4), 386–400.

25 X. Fan, X. Ji, F. Han, J. Yue, J. Chen, L. Chen, T. Deng, J. Jiang and C. Wang, Fluorinated solid electrolyte interphase enables highly reversible solid-state Li metal battery, *Sci. Adv.*, 2018, **4**(12), eaau9245.

26 Z. Huang, S. Choudhury, H. Gong, Y. Cui and Z. Bao, A Cation-Tethered Flowable Polymeric Interface for Enabling Stable Deposition of Metallic Lithium, *J. Am. Chem. Soc.*, 2020, **142**, 21393–21403.

27 J. Wu, Z. Rao, X. Liu, Y. Shen, C. Fang, L. Yuan, Z. Li, W. Zhang, X. Xie and Y. Huang, Polycationic Polymer Layer for Air-Stable and Dendrite-Free Li Metal Anodes in Carbonate Electrolytes, *Adv. Mater.*, 2021, **33**, 2007428.

28 C. Tiyapiboonchaiya, J. M. Pringle, J. Sun, N. Byrne, P. C. Howlett, D. R. MacFarlane and M. Forsyth, The zwitterion effect in high-conductivity polyelectrolyte materials, *Nat. Mater.*, 2004, **3**, 29–32.

29 F. Makhlooghiazad, L. A. O'Dell, L. Porcarelli, C. Forsyth, N. Quazi, M. Asadi, O. Hutt, D. Mecerreyes, M. Forsyth and J. M. Pringle, Zwitterionic materials with disorder and plasticity and their application as non-volatile solid or liquid electrolytes, *Nat. Mater.*, 2022, **21**, 228–236.

30 M. K. Alsaedi, B. D. Like, K. W. Wieck and M. J. Panzer, Zwitterionic Materials for Enhanced Battery Electrolytes, *ChemPlusChem*, 2024, e202300731.

31 G. Li, X. Guan, A. Wang, C. Wang and J. Luo, Cations and anions regulation through zwitterionic gel electrolytes for stable lithium metal anodes, *Energy Storage Mater.*, 2020, **24**, 574–578.

32 L. D. Blackman, P. A. Gunatillake, P. Cass and K. E. S. Locock, An introduction to zwitterionic polymer behavior and applications in solution and at surfaces, *Chem. Soc. Rev.*, 2019, **48**, 757–770.

33 J. Zhu, R. Zhao, J. Zhang, X. Song, J. Liu, N. Xu, H. Zhang, X. Wan, X. Ji, Y. Ma, C. Li and Y. Chen, Long-cycling and High-voltage Solid State Lithium Metal Batteries Enabled by Fluorinated and Crosslinked Polyether Electrolytes, *Angew. Chem., Int. Ed.*, 2024, e202400303.

34 C. Liu, S. Wang, X. Wu, S. Xiao, C. Liu, H. Cai and W.-Y. Lai, In Situ Construction of Zwitterionic Polymer Electrolytes with Synergistic Cation–Anion Regulation Functions for Lithium Metal Batteries, *Adv. Funct. Mater.*, 2024, **34**, 2307248.

35 S. Liu, H. Cheng, R. Mao, W. Jiang, L. Wang, Z. Song, M. Pei, T. Zhang and F. Hu, Designing Zwitterionic Gel Polymer Electrolytes with Dual-Ion Solvation Regulation Enabling Stable Sodium Ion Capacitor, *Adv. Energy Mater.*, 2023, **13**, 2300068.

36 Q. Zhou, C. Fu, R. Li, X. Zhang, B. Xie, Y. Gao, G. Yin and P. Zuo, Poly (vinyl ethylene carbonate)-based dual-salt gel polymer electrolyte enabling high voltage lithium metal batteries, *Chem. Eng. J.*, 2022, **437**, 135419.

37 F. Mo, H. Ren, S. Chen and Z. Ge, Novel zwitterionic polyurethanes with good biocompatibility and antibacterial activity, *Mater. Lett.*, 2015, **145**, 174–176.

38 Y. Jiang, Y. Song, X. Chen, H. Wang, L. Deng and G. Yang, In situ formed self-healable quasi-solid hybrid electrolyte network coupled with eutectic mixture towards ultra-long cycle life lithium metal batteries, *Energy Storage Mater.*, 2022, **52**, 514–523.

39 J. B. Goodenough and Y. Kim, Challenges for Rechargeable Li Batteries, *Chem. Mater.*, 2010, **22**, 587–603.

40 S. Horiuchi, H. Zhu, M. Forsyth, Y. Takeoka, M. Rikukawa and M. Yoshizawa-Fujita, Synthesis and evaluation of a novel pyrrolidinium-based zwitterionic additive with an ether side chain for ionic liquid electrolytes in high-voltage lithium-ion batteries, *Electrochim. Acta*, 2017, **241**, 272–280.

41 S. D. Jones, H. Nguyen, P. M. Richardson, Y.-Q. Chen, K. E. Wyckoff, C. J. Hawker, R. J. Clément, G. H. Fredrickson and R. A. Segalman, Design of Polymeric Zwitterionic Solid Electrolytes with Superionic Lithium Transport, *ACS Cent. Sci.*, 2022, **8**, 169–175.

42 T. Dong, H. Zhang, R. Hu, P. Mu, Z. Liu, X. Du, C. Lu, G. Lu, W. Liu and G. Cui, A rigid-flexible coupling poly(vinylene carbonate) based cross-linked network: A versatile polymer platform for solid-state polymer lithium batteries, *Energy Storage Mater.*, 2022, **50**, 525–532.

43 J. Zhu, J. Zhang, R. Zhao, Y. Zhao, J. Liu, N. Xu, X. Wan, C. Li, Y. Ma, H. Zhang and Y. Chen, In situ 3D crosslinked gel polymer electrolyte for ultra-long cycling, high-voltage, and high-safety lithium metal batteries, *Energy Storage Mater.*, 2023, **57**, 92–101.

44 M. T. Nguyen and Q. Shao, Effects of zwitterionic molecules on ionic association in ethylene oxide-based electrolytes, *Fluid Phase Equilib.*, 2020, **515**, 112572.

45 Y. Jiang, L. Chai, L. Deng and G. Yang, Rationally Designed Fluorinated Polycation Electrolytes for High-Rate, Dendrite-Free Lithium Metal Batteries, *ACS Appl. Mater. Interfaces*, 2023, **15**, 44848–44858.

46 T. Hou, K. D. Fong, J. Wang and K. A. Persson, The solvation structure, transport properties and reduction behavior of carbonate-based electrolytes of lithium-ion batteries, *Chem. Sci.*, 2021, **12**, 14740–14751.

47 T. Hou, G. Yang, N. N. Rajput, J. Self, S.-W. Park, J. Nanda and K. A. Persson, The influence of FEC on the solvation structure and reduction reaction of $LiPF_6$/EC electrolytes and its implication for solid electrolyte interphase formation, *Nano Energy*, 2019, **64**, 103881.

48 Y. Zhang, F. Li, Y. Cao, M. Yang, X. Han, Y. Ji, K. Chen, L. Liang, J. Sun and G. Hou, Tuning the FEC-Related Electrolyte Solvation Structures in Ether Solvents Enables High-Performance Lithium Metal Anode, *Adv. Funct. Mater.*, 2024, 2315527.

49 Z. Li, Y. Chen, X. Yun, P. Gao, C. Zheng and P. Xiao, Critical Review of Fluorinated Electrolytes for High-Performance Lithium Metal Batteries, *Adv. Funct. Mater.*, 2023, **33**, 2300502.

50 X. Pei, Y. Li, T. Ou, X. Liang, Y. Yang, E. Jia, Y. Tan and S. Guo, Li–N Interaction Induced Deep Eutectic Gel Polymer Electrolyte for High Performance Lithium-Metal Batteries, *Angew. Chem., Int. Ed.*, 2022, **61**, e202205075.

51 W. Zhang, T. Yang, X. Liao, Y. Song and Y. Zhao, All-fluorinated electrolyte directly tuned Li^+ solvation sheath enabling high-quality passivated interfaces for robust Li metal battery under high voltage operation, *Energy Storage Mater.*, 2023, **57**, 249–259.

52 S. Han, B. Wu, H. Wang, P. Wen, L. Zhang, X. Lin and M. Chen, Designing F/P Hybrid Polymer as Ultrastable Cationic Shielding Interphase for High-Performance Lithium Metal Batteries, *Angew. Chem., Int. Ed.*, 2023, **62**, e202308724.

53 S. Li, H. Yang, M. Geng, H. Do and C. Peng, Molecular-Level Anion and Li^+ Co-Regulation by Amphoteric Polymer Separator for High-Rate Stable Lithium Metal Anode, *Nano Lett.*, 2024, **24**, 486–492.

54 A. J. D'Angelo and M. J. Panzer, Decoupling the Ionic Conductivity and Elastic Modulus of Gel Electrolytes: Fully Zwitterionic Copolymer Scaffolds in Lithium Salt/Ionic Liquid Solutions, *Adv. Energy Mater.*, 2018, **8**, 1801646.

55 D. Zhang, Y. Liu, Z. Sun, Z. Liu, X. Xu, L. Xi, S. Ji, M. Zhu and J. Liu, Eutectic-Based Polymer Electrolyte with the Enhanced Lithium Salt Dissociation for High-Performance Lithium Metal Batteries, *Angew. Chem., Int. Ed.*, 2023, **62**, e202310006.

56 J. Lopez, D. G. Mackanic, Y. Cui and Z. Bao, Designing polymers for advanced battery chemistries, *Nat. Rev. Mater.*, 2019, **4**, 312–330.

57 W. Wu, D. Li, C. Gao, H. Wu, Y. Bo, J. Zhang, L. Ci and J. Zhang, Eutectogel Electrolyte Constructs Robust Interfaces for High-Voltage Safe Lithium Metal Battery, *Adv. Sci.*, 2024, 2310136.

58 Y. Liang, W. Wu, D. Li, H. Wu, C. Gao, Z. Chen, L. Ci and J. Zhang, Highly Stable Lithium Metal Batteries by Regulating the Lithium Nitrate Chemistry with a Modified Eutectic Electrolyte, *Adv. Energy Mater.*, 2022, **12**, 2202493.